PHOTONICS Research

Direct observation of zero modes in a non-Hermitian optical nanocavity array

Flore Hentinger,[1] Melissa Hedir,[1] Bruno Garbin,[1] Mathias Marconi,[2] Li Ge,[3,4] Fabrice Raineri,[1,5] Juan A. Levenson,[1] and Alejandro M. Yacomotti[1,*]

[1]Centre de Nanosciences et de Nanotechnologies, CNRS, Université Paris-Sud, Université Paris-Saclay, 91120 Palaiseau, France
[2]Université Côte d'Azur, Institut de Physique de Nice, CNRS-UMR 7010, Sophia Antipolis, France
[3]Department of Physics and Astronomy, College of Staten Island, CUNY, Staten Island, New York 10314, USA
[4]Graduate Center, CUNY, New York, New York 10016, USA
[5]Université de Paris, 75205 Paris Cedex 13, France
*Corresponding author: alejandro.giacomotti@c2n.upsaclay.fr

Received 11 August 2021; revised 10 December 2021; accepted 14 December 2021; posted 16 December 2021 (Doc. ID 440050); published 1 February 2022

Zero modes are symmetry protected ones whose energy eigenvalues have zero real parts. In Hermitian arrays, they arise as a consequence of the sublattice symmetry, implying that they are dark modes. In non-Hermitian systems that naturally emerge in gain/loss optical cavities, particle-hole symmetry prevails instead; the resulting zero modes are no longer dark but feature $\pi/2$ phase jumps between adjacent cavities. Here, we report on the direct observation of zero modes in a non-Hermitian three coupled photonic crystal nanocavities array containing quantum wells. Unlike the Hermitian counterparts, the observation of non-Hermitian zero modes upon single pump spot illumination requires vanishing sublattice detuning, and they can be identified through far-field imaging and spectral filtering of the photoluminescence at selected pump locations. We explain the zero-mode coalescence as a parity-time phase transition for small coupling. These zero modes are robust against coupling disorder and can be used for laser mode engineering and photonic computing.

https://doi.org/10.1364/PRJ.440050

1. INTRODUCTION

Majorana zero modes, a captivating concept originally proposed in the study of neutrinos, have intrigued physicists over the past eighty years. Being their own anti-particles and hosting non-Abelian braiding properties, their experimental demonstration is being actively pursued in high-energy physics and condensed matter physics [1–5]. The existence of these zero-energy excitations is warranted by particle-hole symmetry, in the form where the (Hermitian) Hamiltonian anti-commutes with an anti-linear operator [6].

Recently, there have been several proposals to realize particle-hole symmetry in non-Hermitian (NH) systems [7], especially on integrated photonic platforms, where the spatial arrangement of optical gain and loss [8], as well as asymmetric couplings between different elements [9], plays an important role. These findings are quite surprising because photons are bosons and cannot form particle-hole pairs in general. However, by realizing that these effective particles and holes have complex energies in an NH system, they do not need to adhere to Fermi–Dirac statistics as their condensed matter counterparts do. To highlight this difference, we will refer to such symmetries as NH particle-hole (NHPH) symmetry.

Although the resulting zero modes of NHPH symmetry differ from Majorana zero modes in several key aspects, they have two desirable properties in many photonic applications: their symmetry protection not only exists at the origin of the complex energy plane but also extends to the entire imaginary axis; they can also be conveniently excited in standard arrays of optical cavities or waveguides, without requiring the existence of Hermitian counterparts when non-Hermiticity is removed.

Thanks to the flexibility of designing optical elements, these properties of photonic zero modes can also be induced by pseudo-anti-Hermiticity [10]: $\eta H^{\dagger}\eta^{-1} = -H$, where H is the Hamiltonian and η a linear operator. If we consider a system consisting of two sublattices A and B, with K and L waveguides or cavities, respectively, where couplings only take place between two entities belonging to different sublattices, pseudo-anti-Hermiticity coincides with NHPH symmetry when H is symmetric, but it is distinct otherwise, such as in a topological insulator laser [11,12], where an effective gauge field is realized by staggered couplings in a two-dimensional array.

Despite these theoretical advances in the NH domain, the observations of photonic zero modes with the aforementioned properties have been restricted to arrays that resemble their Hermitian counterparts, such as the Su–Schrieffer–Heeger

(SSH) lattice [13–16]. In contrast to topologically protected edge states, the NH zero modes protected by NHPH symmetry, including the ones we study here, are not restricted to interfaces and can be excited in different regions—both bulk and edges—of a coupled photonic array [8]. Let us stress also its simplicity from both the conceptual and technical points of view: an arbitrary number of zero modes can be generated in a large cavity array with arbitrary coupling coefficients by just pumping different sites of an array.

Active photonic crystal (PhC) cavity arrays are outstanding platforms to access the NH realm because they naturally enable *in-situ* realization of gain/loss configurations and coupling engineering [17,18]. A recent demonstration of laser mode switching in a coupled PhC cavity could be explained on the basis of Hermitian dark modes [19]. Remarkably, PhC platforms recently led to the observation of exceptional points (EPs) in two coupled nanocavities [20,21].

In order to show the potential of exciting and controlling a photonic zero mode in a broader range of systems, especially those without a topological origin [8,22], here we report on its observation in a minimal system consisting of three coupled PhC cavities with NHPH symmetry. We will show that the observability of zero modes strongly depends on the frequency detuning between the two extreme cavities (sublattice A) and the central one (sublattice B) in a linear array—which we refer to as sublattice detuning, $\Delta\omega = \omega_B - \omega_A$. In our coupled cavity system, the intercavity coupling g is modified by design, allowing us to feature both large ($|g| \gtrsim |\Delta\omega|$) and small ($|g| < |\Delta\omega|$) coupling regimes. Hereby, we will show that, when entering into the large detuning phase, the zero mode first looses its properties because it is no longer NHPH symmetry protected and eventually coalesces with another lattice mode through a parity-time (PT) phase transition.

This paper is organized as follows. In Section 2, we provide a simple theoretical framework based on coupled mode theory (CMT) to understand zero modes in gain/loss cavity arrays warranted by NHPH symmetry. In Section 3, we describe our PhC three-cavity array with controllable coupling by means of the so-called barrier engineering technique. We also provide an experimental characterization of the linear Hermitian modes through resonant scattering experiments. In Section 4, we move into NH mode characterization by incoherently pumping the system, and we report on the direct observation of the zero mode in the small sublattice detuning regime. Such observation is based on photoluminescence (PL) intensity maps under the spatial scanning of the pump spot combined with a Fourier imaging technique. Conclusions are given in Section 5.

2. THEORETICAL BACKGROUND: NON-HERMITIAN ZERO MODES

A simple theoretical modal analysis of evanescently coupled cavity lattices can be carried out in the framework of the CMT formalism. In the case of N resonant optical cavity lattices, the CMT is valid under the hypothesis of negligible coupling between non-adjacent cavities and weak coupling overall. It assumes that the system can be accurately described with both the isolated (real) cavity frequencies ω_n and the coupling strength to their neighboring cavities. The resulting hybrid mode frequencies and field distributions become the eigenvalues and eigenvectors of a Hamiltonian operator $\tilde{H}$, which does not need to be Hermitian. This is naturally the case of optical cavities in the presence of loss and/or gain [7]: a lattice can be described in CMT by a Hamiltonian $\tilde{H}$ whose matrix elements are $\tilde{H}_{nn} = \tilde{\omega}_n$ and $\tilde{H}_{nm} = g_{nm}$ $(n \neq m)$, where $\tilde{\omega}_n$ are the complex frequencies of the isolated cavities, and g_{nm} are the nearest-neighbor intercavity coupling parameters. In a closed Hermitian system, $\tilde{\omega}_n = \omega_n$ are real, while in an NH gain/loss optical system, $\tilde{\omega}_n = \omega_n - i/\tau_n$, where τ_n is the nth cavity lifetime, which can be negative for net gain. Also, g_{nm} can become complex in general in an NH framework [23]; here, we will consider real g_{nm} for simplicity, i.e., we will neglect mode-loss splitting [17,24].

A zero mode that can be realized in photonics is often the result of the sublattice (or chiral) symmetry in Hermitian lattices, where eigenvalues are real. Indeed, it can be shown that, in Hermitian chiral arrays, the Hamiltonian anti-commutes with a diagonal matrix $\mathcal{C}$ consisting of K ones followed by L minus ones, i.e., $\{\tilde{H}, \mathcal{C}\} = 0$. This property ensures $\varepsilon_k = -\varepsilon_j$, and a zero mode with $j = k$ verifies $\varepsilon_j = 0$. These are known as dark modes, because the intensity in one of the sublattices vanishes [8]. On the other hand, eigenvalues are complex in general in NH arrays. While chiral symmetry can still be realized in this case [6], a more prevailing symmetry that leads to a zero mode in an NH lattice is NHPH symmetry. While sharing key features with their Hermitian counterparts such as the immunity to coupling disorder, they possess an important property: they can exist along the entire imaginary axis. This is warranted provided that $\{\tilde{H}, \mathcal{CT}\} = 0$, with $\mathcal{T}$ being the time-reversal operator, i.e., the system features NHPH symmetry. Zero modes in this framework ($\varepsilon_k = -\varepsilon_j^*$) are not restricted to interfaces and can be excited in different regions—both bulk and edges—of a coupled photonic array. Table 1 summarizes similarities and differences between Hermitian and NH zero modes.

Although our analysis can be extended to large cavity networks, in this work, we will focus on a small array of three coupled cavities as the minimal system containing a zero mode. Figure 1 illustrates a simple case where three cavities are aligned along the x direction, while the resonant intracavity field oscillates back and forth in the y direction [see schematics in Fig. 1(c)]. We assume they all have the same resonant frequency ω_0 chosen as the reference frequency, nearest-neighbor coupling $g_{nm} = g$, and intrinsic field decay time τ_0 due to optical losses. Let us point out that the zero mode has the same frequency as a standalone cavity. One of the extreme cavities, say the top one, is incoherently pumped, therefore introducing a variable gain γ; see Fig. 1(a). The complex eigenvalues of $\tilde{H}$ and their evolution with increasing γ are depicted in Fig. 1(b). The black symbols correspond to the eigenvalues ε_j $(j = 1, 2, 3)$ evolving as the pump is increased from $\gamma = 0$ (red square at the starting point) to $\gamma = 9.3$ (black cross at the end point). We call M1 and M3 the lowest and highest frequency modes, respectively, both having a nearly symmetric field distribution, while M2 is the central mode featuring $\pi/2$ phase jumps between adjacent cavities [Fig. 1(b), inset].

Table 1. Comparative Table with the Salient Properties of Hermitian and Non-Hermitian Photonic Zero Modes

	Hermitian	Non-Hermitian
Definition	$\varepsilon_j = 0$	$\mathrm{Re}(\varepsilon_j) = 0$
Symmetry of the entire spectrum	Chiral ($\varepsilon_k = -\varepsilon_j$)	Non-Hermitian particle-hole ($\varepsilon_k = -\varepsilon_j^*$)
Dimension of existence in the complex plane	0D (at the origin)	1D (along the imaginary axis)
Wavefunction	Dark on one sublattice	$\pi/2$ phase shift between sublattices
Excitation method	Resonant excitation (fluorescence)	Resonant excitation or incoherent pumping (lasing zero mode)
Robustness against	Coupling disorder	Coupling disorder and/or gain/loss disorder

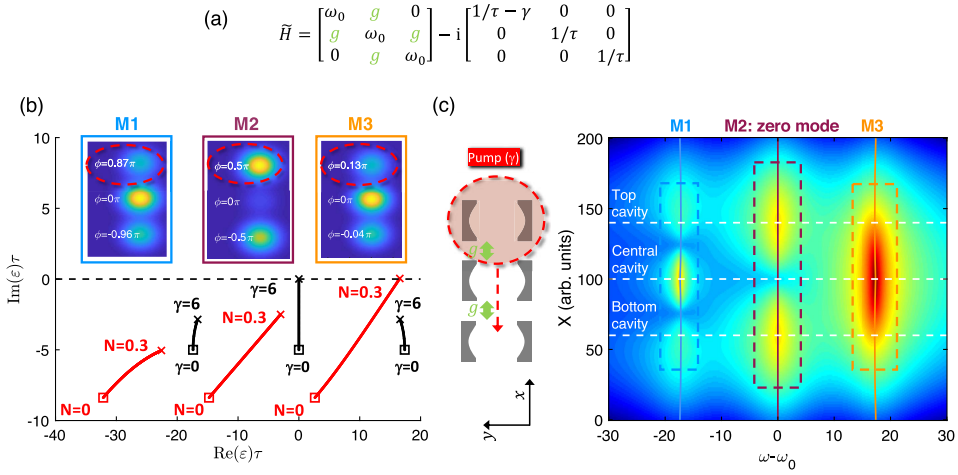

Fig. 1. NH zero mode in a three coupled cavities array: CMT model. (a) NH Hamiltonian. (b) Black symbols and lines: eigenvalues in the CMT model with $\tau_0 = 0.2$ and $g = 12.3$ (inset: intensity and phase spatial distribution at M2 laser threshold). Red symbols and lines: eigenvalues in the CD-CMT model, for increasing carrier density N with a Gaussian profile $N(x;x_1) = \exp[-(x-x_1)^2/\sigma^2]N$ centered at cavity 1 ($\tau_c = 7$ ps, $x_1 = 60$, $\sigma = 50$, $\alpha_H = 2$; other parameters can be found in Appendix A). (c) Logarithmic spectral intensity as a function of the center of a Gaussian pump spot, computed from Eq. (2) in the text. The pump spot profile is $P(x;X) = \exp[-(x-X)^2/\sigma^2]$, and $\gamma_n(X) = P(x_n;X)$, with $\sigma = 50$ and $\gamma = 6$, i.e., below laser threshold. Solid lines correspond to $\mathrm{Re}(\varepsilon_j)$ for $j = 1$ (M1, blue), $j = 2$ (M2, burgundy), and $j = 3$ (M3, orange).

A zero mode ($j = k$), which always exists in the case of an odd number of cavities, leads to $\mathrm{Re}(\varepsilon_j) = 0$. This is the case of M2, whose frequency does not depend on γ because of the NHPH symmetry protection, while M1 and M3 frequencies do. It is worthwhile noting that such a frequency change for M1 and M3 is a pure MH effect, not related to any nonlinear refractive index effect.

Unlike the Hermitian counterparts, the zero mode is no longer a dark one under single cavity pumping; see Table 1 and Fig. 1(b): no light extinction occurs in the central cavity. However, the exact $\pi/2$ phase shift between adjacent cavities distinguishes the wave function of a zero mode from all other modes and dramatically impacts the PL far-field imaging in experiments, as will be shown later on.

Here, we will restrict our analysis to the spontaneous emission regime—i.e., below laser threshold and neglecting amplification—in which a linear NH CMT is valid. We assume a (Gaussian) pump spot profile $P(x;X)$ centered at a given X position; therefore, $\gamma_n(X) = P(x_n;X)$, where x_n are the central positions of the cavities. As a result, ε_j depends not only on the pump power but also on the pump position, $\varepsilon_j = \varepsilon_j(X)$. The spontaneous emission in the cavities is $|f\rangle$ ($f_n \propto \gamma_n$), and the modal excitation amplitudes $f_j(X) = \langle \Phi_j | f \rangle$, with $|\Phi_j\rangle$ being the left eigenvectors of $\tilde{H}$. In this spontaneous emission regime, the total emitted spectral intensity can be calculated as the incoherent superposition of the N mode intensities, each one contributing with a Lorentzian peak of amplitude $f_j(X)$, resonant frequency $\mathrm{Re}[\varepsilon_j(X)]$, and width $\mathrm{Im}[\varepsilon_j(X)]$:

$$I(\omega;X) = \left| \sum_j \frac{f_j(X)}{\{\omega - \mathrm{Re}[\varepsilon_j(X)]\}i + \mathrm{Im}[\varepsilon_j(X)]} \right|^2, \quad (1)$$

$$I(\omega;X) \simeq \sum_j \frac{|f_j(X)|^2}{\{\omega - \mathrm{Re}[\varepsilon_j(X)]\}^2 + \{\mathrm{Im}[\varepsilon_j(X)]\}^2}. \quad (2)$$

Figure 1(c) shows the spectral intensity map $I(\omega;X)$ under spatial scanning of a Gaussian pump spot, computed from Eq. (2). The signatures of the zero mode are the two central lobes corresponding to M2 in Fig. 1(c). Such an intensity map, together with systematic far-field measurements, constitutes a tool to experimentally investigate zero-mode radiation in the active cavity array.

NH zero modes warranted by NHPH symmetry have the freedom to evolve along the $\mathrm{Im}(\varepsilon)$ axis. In particular, at

$\gamma = 9.3$, $\mathrm{Im}(\varepsilon_2) = 0$ so that the gain compensates the losses. Thus, the linear CMT model predicts zero-mode lasing in three coupled cavities systems as one of the extreme cavities is pumped [8]. When dealing with active semiconductor media—such as InP membranes with quantum wells (QWs), as in our experiments—an important deviation from this simple CMT model is the absorption saturation and carrier-induced refractive index changes below the laser threshold, leading to frequency blue shifts of the cavity mode. We have incorporated those effects in the CMT model, which we call hereafter carrier-dependent CMT (CD-CMT) equations, derived in Appendix A. In essence, these are based on a logarithmic model for the absorption and the refractive index as a function of the charge carrier density in the QWs. The eigenvalues as a function of the carrier are superimposed to the linear CMT eigenvalues in Fig. 1(b) (red symbols and lines). It can be observed that it is now the highest energy eigenvalue M3 that reaches the threshold before the middle one M2. Qualitatively, lasing phenomena require a good spectral and spatial overlap between the gain and the optical mode. Since the pump-induced refractive index effect blue shifts the optical mode of the pumped cavity, it is likely that the closest hybrid mode to the blue-detuned pumped cavity will be more efficiently excited. This qualitative argument is translated in the evolution of the eigenvalues, as evidenced in Fig. 1(b).

3. THREE COUPLED PHOTONIC CRYSTAL CAVITIES: DESIGN AND CHARACTERIZATION OF HERMITIAN MODES

PhC cavities with embedded QWs are a suitable platform to experimentally investigate zero-mode photonics. This is due to the multiple degrees of freedom provided by the design parameters, as well as the intrinsic and controllable gain/absoption features.

Three coupled PhC L3 cavities [three missing holes in the ΓK direction of a triangular air hole lattice, see Fig. 2(a)] are separated by three rows of holes in the ΓM direction, leading to evanescent coupling. The two extreme cavities of the linear array couple to the middle cavity through a coupling coefficient g. In order to control g, we implement the so-called barrier engineering technique, by virtue of which the coupling strength (and even its sign) can be changed, modifying the middle row separating two adjacent cavities [17,18]. We have designed the central hole row in the barriers with radius $r_3 = r_0(1 + h)$, with r_0 being the hole radius of the underlying PhC lattice. We call the parameter h the barrier perturbation. Importantly, h has a strong impact on the cavity frequencies due to its influence on the effective refractive index surrounding the cavities. Since the barrier induces a frequency detuning $\Delta\omega(h)$ in a contiguous nanocavity, a good approximation is to consider the two extreme cavities as having the same frequency $\omega_0 + \Delta\omega(h)$ and $\omega_0 + 2\Delta\omega(h)$ for the central cavity [see schematics in Fig. 2(a), bottom and Appendix C for further details]. Therefore, the sublattice detuning is $\Delta\omega = \omega_B - \omega_A \approx \Delta\omega(h)$.

In order to predict the influence of the barrier parameter in the coupled mode structure, we have carried out 3D finite difference time domain (FDTD) simulations. First, $g(h)$ and $\Delta\omega(h)$ have been obtained by polynomial fitting datasets of a two coupled cavity system separated by a barrier with perturbation h (see Fig. 5 in Appendix B). Importantly, two regions of h can be distinguished: the large detuning region, $|\Delta\omega(h)| > |g(h)|$ for $h \leq -5\%$ or $h \geq 10\%$, and the small

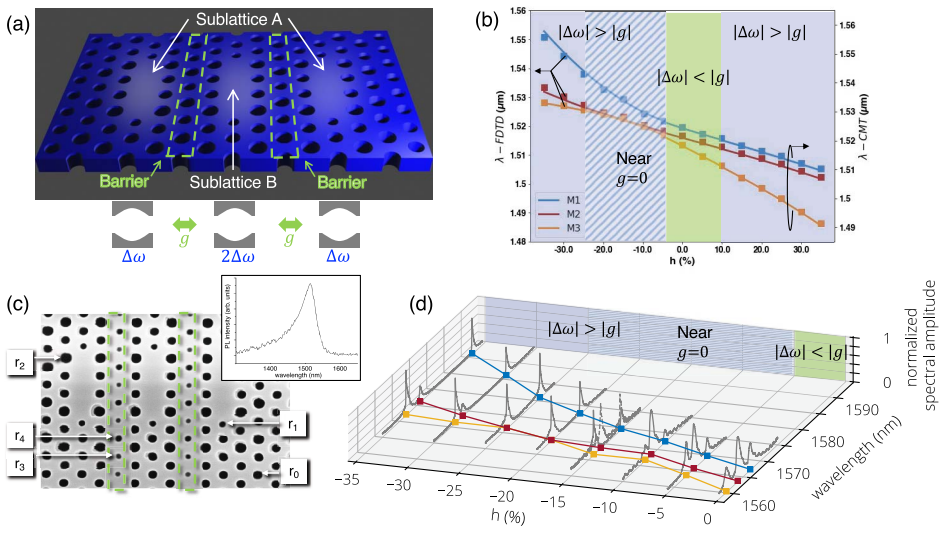

Fig. 2. Three coupled PhC cavities. (a) Artist view of the system, featuring controllable coupling by means of the two barriers (highlighted with dashed boxes) in which holes are modified. Two sublattices A and B can be defined, where couplings only take place between cavities belonging to different sublattices. Bottom: schematic representation showing how the presence of the barriers modifies the cavity detuning. The sublattice detuning is then $\Delta\omega$. (b) The 3D-FDTD simulation results of three coupled PhC cavities showing the evolution of the mode resonant wavelengths (symbols, left axis) as a function of the barrier parameter. Solid lines (right axis) are CMT predictions using polynomial approximations of $g(h)$ and $\Delta(h)$ obtained from two coupled cavity FDTD simulations (see Appendix B). Two regions can be distinguished: the low (light green, $|g| \gtrsim |\Delta\omega|$) and high sublattice detuning regions (light blue, $|g| < |\Delta\omega|$); the near-zero coupling region is highlighted with a striped background. (c) SEM image of a sample of three coupled L3 InP-based PhC cavities. Inset: QW PL. (d) Normalized reflectivity spectra as a function of the barrier parameter from resonant scattering experiments. These results can be interpreted as the optical response of the coupled cavity system in the Hermitian limit.

detuning region, $|\Delta\omega(h)| < |g(h)|$ for $-5\% \lesssim h \lesssim 10\%$. Subsequently, 3D-FDTD simulations with three cavities have been carried out. The mode frequencies as a function of h are depicted in Fig. 2(b), together with the Hermitian CMT predictions using the fitted parameters $\Delta\omega(h)$ and $g(h)$ (Appendix C), showing very good agreement.

We have fabricated the PhC cavity array of Fig. 2(a) in a suspended InP membrane of 280 nm thickness containing four $InGa_{0.17}As_{0.76}P$ QWs, featuring a PL peak at $\lambda \approx 1514$ nm [Fig. 2(c)]. The details on the fabrication can be found in Ref. [17]. The hole radius is $r_0 = 0.266a$, and a, the period of the triangular lattice, lies in the range of 400–420 nm. The two holes limiting each cavity have a reduced radius of $r_1 = r_0 - 0.06a$ and are displaced away by $s = 0.16a$, in order to increase the Q-factor [25]. Also, holes around the cavities are modified with a period $2a$ by $r_2 = r_0 + 0.05a$ in order to improve the beaming quality of the emitted light and hence the collection efficiency [26]; consequently, beaming holes inside the barrier have radius $r_4 = r_2(1 + h)$. Only samples with $h \leq 0$ have been realized, which suffices to largely tune the intercavity coupling strength g. The resonance wavelengths of the samples range from 1500 to 1600 nm depending on the lattice period. The Q-factor of the cavity resonances is $Q \sim 4000$ at $\lambda = 1580$ nm, i.e., far from the QW absorption.

Two kinds of experimental characterizations have been carried out: reflectivity spectra and PL experiments, both with controlled spatial positions of the illumination spots. For the reflectivity spectra, a single mode tunable laser is used, where the reflected signal is coupled into a single mode optical fiber and sent to a femtowatt photodetector; the background reflectivity is highly suppressed using polarization optics (see Appendix D). In these experiments, the cavity wavelengths, lying in the range of 1560–1600 nm, are red-detuned from the QW absorption, and the illumination power is low enough to be considered as linear reflectivity experiments. Hence, these can be interpreted as optical characterizations of linear Hermitian modes [Fig. 2(d)]. Unlike standard resonant scattering experiments leading to Fano resonances, the reflectivity background suppression allows us to clearly identify modes as Lorentzian-like peaks.

The spectral position of the measured resonances is in very good agreement with the FDTD calculations of Fig. 2(b). Noticiably, three modes are clearly distinguished for $h = 0\%$ and $h = -5\%$, corresponding to the low sublattice detuning region, while the middle peak is not apparent for $-25\% \leq h \leq -10\%$. This interval is within a crossover region where g is small and changes signs [$-25\% \leq h \leq -5\%$ corresponding to -2.17 THz $\leq g \leq 1.26$ THz, dashed region in Fig. 2(b)], with a crossing point ($g = 0$) at $h \approx -15\%$. As a consequence, M2 and M3 frequencies are slightly split in this region. Finally, M2 resonances re-emerge for $h \leq -30\%$. Note that although the system is no longer chiral for $\Delta\omega \neq 0$, M2 remains a zero mode due to geometric frustration, where the couplings from cavities 1 and 3 are canceled in cavity 2 (see Appendix E).

4. DIRECT OBSERVATION OF THE NON-HERMITIAN ZERO MODE

In addition to the reflectivity spectra of the previous section, which characterize Hermitian modes, we have also performed PL experiments, where the pump laser wavelength is now $\lambda = 800$ nm: the laser beam is mainly absorbed in the quantum barriers, and thus it can be considered as an incoherent pump. We use a pulsed laser (100 ps duration and 1 MHz repetition rate) in order to reduce thermal effects. As in the reflectivity experiments, the pump spot is focused down to nearly the diffraction limit so as to achieve a pump configuration with a localized gain profile across the cavity array, meaning that essentially one cavity is pumped when aligning the pump beam at its center. The radiated PL is collected in the free space and spectrally resolved with a spectrometer coupled to an InGaAs one-dimensional (1D) detector array. A piezo-electric-driven stage holding the sample allows us to externally control the sample position with respect to the pump spot with sub-micron resolution. The results are shown in Figs. 3 and 4.

The spectral intensity as a function of the sample position reveals two distinct typical patterns depending on the value of the barrier parameter h. For $h < -5\%$, the detuning $|\Delta\omega(h)|$ is larger than the coupling strength $|g(h)|$; we can then expect that the two extreme cavities become effectively decoupled from the central one, especially for $h \leq -20\%$. The spectral map of Fig. 3(a) ($h = -20\%$) is consistent with this prediction: as long as the pump excites the QWs in one of the extreme cavities, a resonant mode is observed at $\lambda_0 \approx 1558.2$ nm, and, when pumping the middle cavity, a mode red shifted by

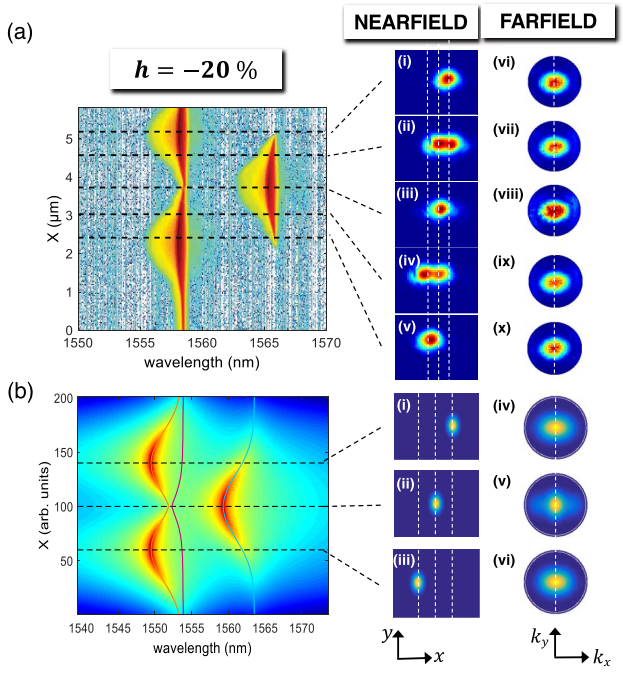

Fig. 3. Spatially resolved PL measurements in the large detuning regime. (a) Experimental results showing spectral intensity maps upon spatial scanning of a pump spot for $a = 416$ nm and $h = -20\%$, $P_{\text{pump}} = 0.8$ μW. The position of the sample is changed by means of the piezo-electric voltage. (b) CD-CMT predictions ($\sigma = 40$, $N = 0.22$, $\alpha_H = 3$). Near-field [(a)-i to (a)-v, (b)-i to (b)-iii] and far-field [(a)-vi to (a)-x, (b)-iv to (b)-vi] images are displayed at the selected pump spot positions marked with horizontal dashed lines. Vertical white dashed lines in the near field indicate the position of the cavities, and $k_x = 0$ in the far field.

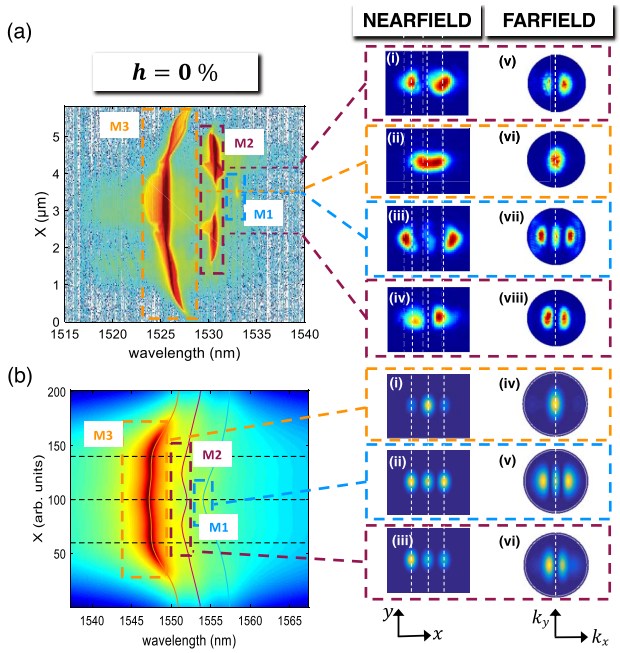

Fig. 4. Observation of the zero mode in the low detuning regime. (a) Experimental results showing spectral intensity maps upon spatial scanning of a pump spot for $a = 408\,\text{nm}$ and $h = 0\%$, $P_{\text{pump}} = 0.8\ \mu\text{W}$. The position of the sample is changed by means of the piezo-electric voltage. (b) CD-CMT predictions ($\sigma = 40$, $N = 0.27$, $\alpha_H = 3$). Near-field [(a)-i to (a)-iv, (b)-i to (b)-iii] and far-field [(a)-v to (a)-viii, (b)-iv to (b)-vi] images are displayed at the selected pump spot positions marked with horizontal dashed lines. Spectral filters are used in order to remove contributions from other modes, the spectral bandwidth being represented by the horizontal extension of dashed boxes. Vertical white dashed lines in the near field indicate the position of the cavities, and $k_x = 0$ in the far field.

$\Delta\lambda \approx 7.7\ \text{nm} \sim 6\ \text{THz}$ comes out, consistent with the $|\Delta\omega(h = -20\%)| \approx 7$ THz detuning obtained from the numerical simulations. The near-field images [Figs. 3(a)-i to 3(a)-v] show that the emission essentially comes from the pumped cavity provided only one mode is excited. Note that two near-field lobes can be observed for intermediate positions, where two resonances are simultaneously present in the spectrum [Figs. 3(a)-ii and 3(a)-iv]. The far-field images [Figs. 3(a)-vi to 3(a)-x] confirm this observation of always revealing only one central lobe, consistent with a localized cavity mode. It is even the case for two near-field lobes, for which the radiation pattern becomes the incoherent superposition of two centered single cavity far-field lobes [Figs. 3(a)-vii and 3(a)-ix].

This analysis allows us to conclude that the two external cavities are decoupled from the central one for large sublattice detuning. The experimental results are in very good agreement with CD-CMT calculations that blue shift the cavity resonance as a function of the pump power.

Interestingly, although the zero mode would still exist in the case of large $\Delta\omega$ in Hermitian systems, it is no longer observable in our NH system with detuning using a single localized pump spot. As pointed out before, this is because Hermitian zero modes are dark ones; therefore, they remain unaffected if the detuning takes place only in the cavities where the amplitude of the zero modes is zero. On the other hand, the NH zero modes are not dark ones in general. Here, in our NH system, a single localized pump spot results in an imaginary detuning that acts together with the real (frequency) detuning to eliminate the NHPH symmetry and its zero modes (see Appendix E). Therefore, within this large sublattice detuning regime, the NH zero mode is destroyed when pumping on one extreme cavity.

To experimentally address a zero mode, we change the barrier parameter to enter into the low detuning regime, $h \sim 0\%$. Within this regime, the spectral intensity pattern totally differs from the large detuning case where localized modes prevailed [Fig. 3(a)]. For $-5\% \lesssim h \lesssim 10\%$, $|\Delta\omega(h)| < |g(h)|$ [Fig. 2(b)] and the three coupled cavities effectively behave as a whole. In the spectral intensity map [Fig. 4(a), $h = 0\%$], we can observe a pattern with the mode of highest energy M3 being excited independently of the sample position; it has a higher intensity compared to the two other modes. The central mode M2, on the other hand, attains two maxima in between the extreme cavities and the central one. The lowest energy mode M1 is the weakest one, and it is only observed when pumping near the central cavity, a feature that was already present in the simplified calculation of Fig. 1(c).

In these conditions, we have measured the near-field and far-field patterns, setting the pump spot positions at the local maxima of the modes and using pass-band filters to filter out all other spectral components. From the near and far-field images of the highest [M3, Figs. 4(a)-ii and 4(a)-vi] and lowest [M1, Figs. 4(a)-iii and 4(a)-vii] energy modes, we conclude that those are approximately symmetric modes, with M1 being the fundamental one, which is in agreement with the CMT and FDTD calculations. In particular, the near-field images [Figs. 4(a)-ii and 4(a)-iii] show that the emission of those two modes comes from all three cavities, with a higher intensity in the middle for M3 and in the extreme ones for M1. The central mode, on the other hand, features a far-field intensity node at the center [M2, Figs. 4(a)-v and 4(a)-viii]; its near field is more intense in the two extreme cavities [Figs. 4(a)-i and 4(a)-iv], while the intensity is below our detection limit in the central cavity region. These observations are compatible with the NH zero mode M2 of Section 2. In particular, the $\pi/2$ phase jump between adjacent cavities predicted for an NH zero mode is translated into a π phase difference between the two extreme cavities, giving rise to an anti-symmetric-like far-field profile, as it has already been observed for two coupled cavities [27].

Figure 4(b) shows the CD-CMT calculations. The carrier-induced refractive index effects have an important impact on the PL map, as compared to Fig. 1(c). Although the main qualitative features are already captured by a linear NH CMT, in the CD-CMT, the blue-detuned mode M3 strongly dominates over the other two modes. As discussed before, this can be explained as a consequence of the frequency blue shift of a cavity resonance under optical pumping: we can therefore expect that the blue most detuned hybrid mode will be more efficiently excited, since its spectral overlap with the pumped cavity resonance increases. This explains the enhancement of the

high-energy mode M3 in this low sublattice detuning regime, even though the zero mode is clearly observable. Compared to the experimental result of Fig. 4(a), the two M2 lobes are less visible; this might be due to the simplification of our CD-CMT model that neglects dissipative coupling and amplification. Importantly, the zero mode might be brought to laser operation as long as a two spot pumping scheme is implemented (see Appendix E), as will be reported elsewhere. In addition, in our carrier-dependent model, we observe that the intercavity phase jumps in M2 become quite sensitive to frequency shifts; in the CD-CMT calculation of Fig. 1(b), the M2 cavity phases for $N = 0.3$ are $[0.85\pi, 0, 1.85\pi]$, thus deviating from the expected $\pi/2$. Such sensitivity is a further example of how active semiconductor media, featuring a carrier-induced refractive index, may have a significant impact in the NH realm. For instance, in PT-symmetry breaking experiments using semiconductor microcavities, PT symmetry gets explicitly broken in the sense that the real part of the permittivity is no longer symmetric under asymmetric pumping.

Let us now address the question of the extinction of the NH zero mode in this system for decreasing the h parameter. First, we notice that for very small $|g|$ PT-symmetry breaking is predicted as one extreme cavity is pumped. Within this broken PT-symmetry phase ($-18\% < h < -11\%$), the central cavity (sublattice B)—already effectively decoupled from the two extreme ones—does not play an important role; at the same time, the two extreme ones (sublattice A) weakly interact with each other, such that a gain imbalance may undergo an EP. This is depicted in Figs. 7(l) and 7(m) of Appendix F: the real parts of the eigenvalues of modes M2 and M3 undergo EPs when pumping in the proximity of an extreme cavity. Within a pumped cavity of sublattice A, as it is apparent in the inset of Fig. 7(l), the real parts of the eigenvalues of M2 and M3 coalesce in a single branch; there, only one mode is observable—the one with higher gain—and it is localized in the pumped cavity. The otherwise EP bifurcation results in an imperfect symmetry breaking [Figs. 7(g) and 7(h)] [28], enhancing light localization in the pumped cavity. Therefore, within this broken PT-symmetry region, light localization in the real device is a combination of underlying PT-symmetry breaking and pump-induced frequency shift effects, while outside this region [Figs. 7(a), 7(f) and 7(k)] localization in one extreme cavity arises because of pure carrier-induced refractive index effects.

5. CONCLUSION

We have reported on the direct observation of NH zero modes warranted by NHPH symmetry in a minimal cavity array: three coupled PhC nanocavities in a gain/loss configuration under spatially localized optical pumping. Because the number of cavities is odd, Lieb's theorem ensures the existence of a zero mode in the Hermitian limit, which evolves continuously into an NH zero mode. Therefore, there is no need to generate it through, for instance, NHPH spontaneous symmetry restoration. These two types of zero modes do not transform into each other in general (except at a higher-order EP [29]) and can hence be regarded as topologically distinct.

The nature and properties of these NH zero modes differ from their chiral Hermitian counterparts in two main aspects. First, unlike Hermitian zero modes, NH ones are more robust in the sense that they are not restricted to the origin of the complex plane, but they may exist along the imaginary axis, still benefiting from symmetry protection. More specifically, and analogously to chiral modes, they are immune to random coupling perturbations in the cavity array. Second, although NH zero modes are not dark ones in general, in the sense that there is no light extinction in one of the sublattices, these zero modes feature $\pi/2$ phase jumps between adjacent cavities. These constitute unambiguous physical signatures that distinguish their wavefunctions from any other ones in the array and enable experimental protocols to detect them. Here, we have shown that a PL intensity map under spatial scanning of the pump spot provides a clear fingerprint of zero modes in the form of PL maxima in between cavities. At those PL maxima, a Fourier imaging technique allows us to identify nodes at the far-field center ($k = 0$) due to a π-phase difference between the extreme cavities, compatible with the predicted $\pi/2$ phase jumps.

We have identified different regimes that arise as the coupling barrier of the photonic molecule is systematically modified through the perturbation parameter h that varies the hole radius of a row within the photonic barrier. Such a barrier modification simultaneously changes the coupling g and the sublattice detuning $\Delta\omega$, giving rise to two important regimes: $|\Delta\omega| > |g|$ leading to sublattice localization and $|\Delta\omega| < |g|$ leading to sublattice delocalization and zero modes. Remarkably, we have identified the transition from zero-mode observation to its extinction as h is decreased as a combination of underlying PT-symmetry breaking and carrier-induced blue shift effects, which strongly localize the PL in a single cavity.

In spite of the tremendous theoretical advances in the NH domain, observations of photonic zero modes have been restricted so far to waveguide or cavity arrays that resemble their Hermitian counterparts, such as the SSH lattice. Although experimental demonstrations of NH phenomena such as PT-symmetry breaking and EPs are coming to maturity, with special focus in two resonator systems, the physical realization of NH symmetries beyond PT such as NHPH in large cavity arrays—a unique playground for NH photonics—is still in its infancy. We believe that further developments in this direction would enable promising applications of NH symmetry protected modes, ranging from laser array mode engineering, optical communications, and photonic computing [30]. For instance, one can imagine expanding the number of optical communication channels without requiring additional bandwidth, using instead the different spatial profiles of these modes as an additional degree of freedom. This approach provides an alternative or complement to encoding optical signals using beams with different orbital angular momentum [31], which has gained fast-growing interest in the past decade.

APPENDIX A: CARRIER-DEPENDENT CMT MODEL

We will consider CMT of an optical cavity filled with a QW material as a more realistic model of our experiments as compared to a linear NH CMT model. As a matter of fact, optically

pumping a PhC membrane containing QWs produces not only absorption saturation and gain—nonlinear with the pump intensity, but also blue shift of the resonant mode due to carrier-induced refractive index effects. For a single active cavity, we use a standard CMT equation describing the temporal dynamics of the field amplitude a:

$$\frac{\mathrm{d}a}{\mathrm{d}t} = -a\left[\frac{1}{\tau_c} + \frac{1}{\tau_a(N)}\right] + ia[\omega_c + \Delta\omega_{\mathrm{QW}}(N)], \tag{A1}$$

with τ_c (ω_c) the photon lifetime (resonant frequency) of the bare cavity, τ_a the absorption lifetime ($\tau_a < 0$ in the presence of gain), $\Delta\omega_{\mathrm{QW}}$ the QW carrier-induced frequency shift, and N the carrier density. Using perturbation theory, it is possible to relate both the absorption and frequency shift to the imaginary and real parts of the QW electrical susceptibility $\chi_{\mathrm{QW}}(N)$, respectively, in the following way:

$$\frac{1}{\tau_a(N)} = \frac{v_{g0}\omega_c\Gamma}{2cn_r}\Delta\chi''_{\mathrm{QW}}(N),$$
$$\Delta\omega_{\mathrm{QW}}(N) = -\frac{\omega_c\Gamma}{2n_r^2}\Delta\chi'_{\mathrm{QW}}(N), \tag{A2}$$

where v_{g0} is the group velocity of the uniform slab, Γ is the optical confinement factor of the cavity (here, $\Gamma = 0.2$), and n_r is the effective refractive index of the slab (here, $n_r = 3$).

Noting that the imaginary part of the QW susceptibility can be related to the QW absorption $\alpha(N)$ through $\alpha(N) = (\omega_c/cn_r)\Delta\chi''_{\mathrm{QW}}(N)$ and approximating

$$\frac{\Delta\chi'_{\mathrm{QW}}(N)}{\Delta\chi''_{\mathrm{QW}}(N)} \approx \frac{\partial\chi'_{\mathrm{QW}}/\partial N|_{N_0}}{\partial\chi''_{\mathrm{QW}}/\partial N|_{N_0}} \equiv \alpha_H(N_0),$$

where N_0 is the carrier density at QW transparency, and α_H is the so-called Henry factor of the semiconductor laser—also known as the linewidth enhancement factor, Eq. (A2) can be written as

$$\frac{1}{\tau_a(N)} = \frac{v_{g0}\Gamma}{2}\alpha(N),$$
$$\Delta\omega_{\mathrm{QW}}(N) = -\frac{v_{g0}\Gamma}{2}\alpha(N)\alpha_H(N_0).$$

The QW absorption can be approximated by the following phenomenological logarithmic function of N:

$$\alpha(N) = -\frac{\omega_c}{n_r c}\ln\left(\frac{N+A}{N_0+A}\right), \tag{A3}$$

where N_0 is the carrier density at QW transparency, and A is a phenomenological parameter. These have been obtained by fitting experimental data of linewidth as a function of the pump power below laser threshold (not shown) and giving $N_0 = 0.2$ and $A = 2.5$ in normalized units. In addition, measurements of the spectral shift as a function of the pump power led to $\alpha_H(N_0) \equiv \alpha_H \sim 2.5$–$3$, approximately independent of the pump power and, hence, of the carrier density.

APPENDIX B: 3D-FDTD SIMULATIONS

3D-FDTD simulations have been performed using Lumerical-FDTD Solutions software package. We first simulated the case of two coupled cavities in order to predict the dependence of the coupling on the barrier perturbation h. The simulated structure consists of a 280-nm-thick PhC membrane with a refractive index of $n = 3.17$. The period and hole radius of the lattice are $a = 414$ nm and $r_0 = 0.266a$, respectively. The two end holes of the cavities are separated by $s = 0.16a$, and their radius is reduced to $r_1 = r_0 - 0.06a$. For accurate results, two parameters should be taken into account: the mesh size and the simulation time. Concerning the former, we have verified that a spatial step size of $a/20$ in the x and y directions and $a/10$ in the z direction lead to accurate results. As far as the simulation time is concerned, the results converge with $T = 10$ ps.

We have introduced perfectly matched absorbing layers (PMLs) to overcome the problem of parasitic reflections that can occur in the vicinity of the studied structure. In addition, symmetry boundary conditions are used whenever the electromagnetic fields have a plane of symmetry through the middle of the simulation region. By taking advantage of this symmetry, the simulation volume and time can be reduced. In our simulations, the boundary conditions are PMLs in the x and y directions and symmetric along the z axis.

In order to excite the modes of the coupled system, we have randomly distributed eight magnetic dipoles along each cavity, and the resonant modes are extracted using two types of monitors. For extracting resonant modes, time monitors are placed inside the cavities. These monitors provide time series of field

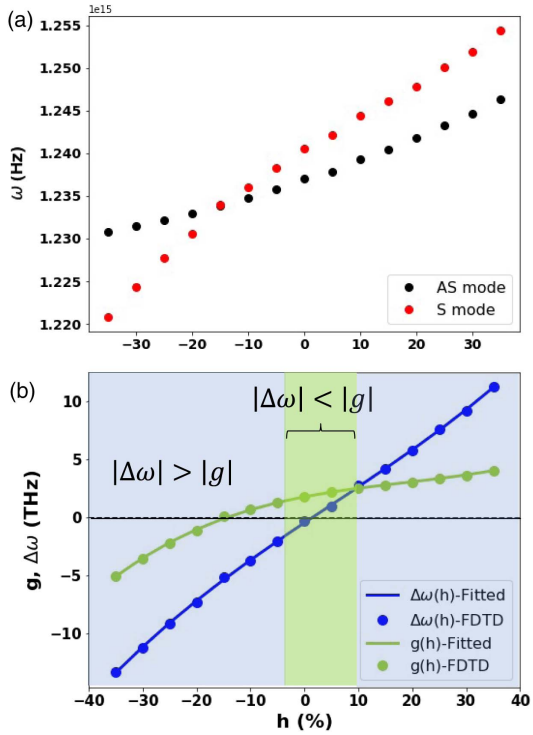

Fig. 5. Two coupled PhC cavities' 3D FDTD numerical simulations as a function of the barrier perturbation parameter h (see main text). (a) Hybrid mode frequencies. (b) Coupling and cavity detuning extracted from the hybrid mode frequency splitting and average, respectively. Solid lines are third-order polynomial fittings, which are subsequently used for CMT calculation with three coupled cavities in the main text.

components throughout the simulation, and, subsequently, the resonance spectrum of the system is obtained through Fourier analysis. In addition to the spectra, the electromagnetic field spatial distribution for each resonance has also been recorded thanks to frequency-domain field monitors, allowing us to distinguish the modes according to their field distributions.

The barrier parameter h has been varied from −0.35 to 0.35. Figure 5(a) illustrates the evolution of the two modes with h. For $h = 0$ (without changing the hole radius of the central row), the anti-symmetric mode is the mode with smaller energy (anti-symmetric ground state), and the situation is reversed for $h < -15\%$, with a mode crossing point at $h \approx -15\%$.

APPENDIX C: POLYNOMIAL FITTING AND LINEAR COUPLED MODE THEORY

As discussed in the main text, the changing of h affects not only the coupling strength g but also the coupled cavity resonant frequencies, which exhibit an offset with that of a single cavity ($\omega_0 = 1.2391 \times 10^{15}$ Hz) by an amount $\Delta\omega$. In order to find approximated expressions of $\Delta\omega(h)$ and $g(h)$ to be eventually used in our CMT formalism for three coupled cavities, we first consider the following CMT Hamiltonian as a model for the two coupled cavity system simulated in the previous section:

$$H = \begin{pmatrix} \omega_c - \frac{i}{\tau} & g \\ g & \omega_c - \frac{i}{\tau} \end{pmatrix},$$

where g, ω_c, and $\tau \in \mathbb{R}$. Note that we assume the cavities to be identical and the coupling to be lossless. We calculate analytically $\det(H - \omega\overleftrightarrow{\Pi}) = 0$ to get the system eigenvalues:

$$\omega_\pm = \omega_c \pm g - i\frac{1}{\tau},$$

where $\omega_\pm$ corresponds to the symmetric (anti-symmetric) modes. The mode frequencies are given by $\mathrm{Re}(\omega_\pm) = \omega_c \pm g$. We define the resonant cavity frequency ω_c as the frequency of an isolated cavity (ω_0) plus a detuning $\Delta\omega$, so that the eigenfrequencies become

$$\mathrm{Re}(\omega_\pm) = \omega_0 + \Delta\omega(h) \pm g(h). \tag{C1}$$

From Eq. (C1) and the data in Fig. 5(a), we calculated $\Delta\omega(h)$ and $g(h)$. The results are represented in Fig. 5(b) together with the following third-order polynomial fits:

$$\Delta\omega(h) = 3.2252 \times 10^{13} \times h^3 - 5.1235 \times 10^{12} \times h^2 + 3.1162 \times 10^{13} \times h - 4.7566 \times 10^{11},$$

$$g(h) = 3.3261 \times 10^{13} \times h^3 - 1.8775 \times 10^{13} \times h^2 + 8.9617 \times 10^{12} \times h + 1.7609 \times 10^{12}.$$

Armed with these expressions for $\Delta\omega$ and g, we can now predict the behavior of the modes in a system of three coupled cavities as a function of the barrier parameter. First, we have simulated one cavity in the presence of one barrier at a side and two barriers [Fig. 6(a)]. We observe that, in the latter case, the wavelength shift is twice that of the one with only one barrier. In addition, the Q-factor also follows a similar rule when adding a barrier at a side, implying the additional leakage is doubled; however, the perturbation in the total Q-factor being small (∼10%), we can neglect the effect in the losses. Therefore, we will assume that, in the three-cavity system,

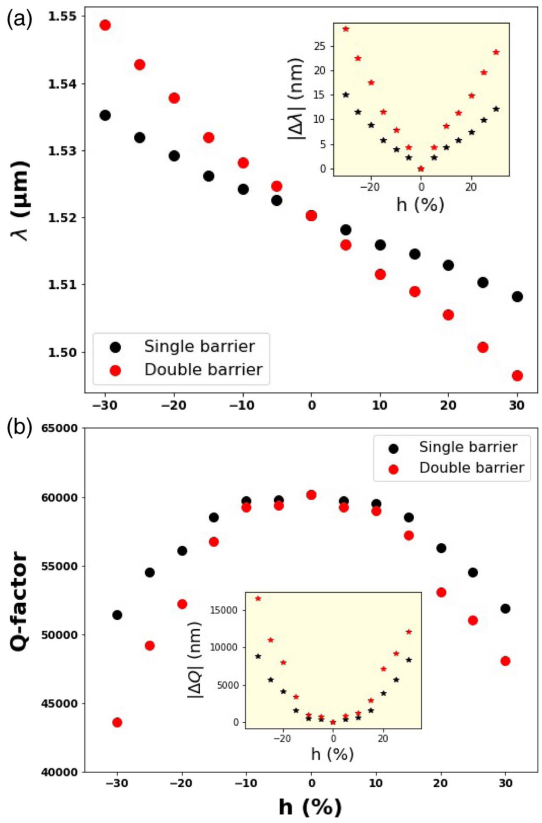

Fig. 6. Single PhC cavity 3D FDTD numerical simulations in the presence of one or two barriers at the sides.

the frequency detuning of the middle cavity is twice the detuning of the extreme ones, which leads to the real Hamiltonian of Eq. (C2):

$$H = \begin{pmatrix} \omega_0 + \Delta\omega(h) & g(h) & 0 \\ g(h) & \omega_0 + 2 \times \Delta\omega(h) & g(h) \\ 0 & g(h) & \omega_0 + \Delta\omega(h) \end{pmatrix}. \tag{C2}$$

The eigenvalues of Eq. (C2) are shown in Fig. 2(b) of the main text, together with 3D-FDTD numerical simulations of three coupled cavities, where the latter have been obtained with the same simulation parameters as the ones described in the previous section.

APPENDIX D: LINEAR REFLECTIVITY EXPERIMENTS

We characterize the behavior of the linear Hermitian modes in our system by performing linear reflectivity experiments as briefly described in the main text. The quasi-resonant injection beam is obtained from a Tunics T100s-HP, and its polarization is managed by means of a polarizing beam splitter combined to a subsequent half-wave plate that ensures linear horizontal polarization. The injection beam reaches the injection/detection beam splitter (80% reflectivity) and a half-wave plate and is finally injected through a 0.95 numerical aperture

microscope objective (Olympus MPLAN 100× IR). The fast axis of the half-wave plate is rotated at 22.5° from the injection beam, allowing an injection at 45° from the cavity polarization and an according polarization separation between the non-injected and the injected beams. An additional lens with 100 cm focal length is located prior to injection so as to facilitate mode matching with the cavities. We then separate the non-injected and injected beams after the injection/detection beam splitter using a half-wave plate—in order to select the detected polarization—and a polarizing beam splitter. We finally inject a monomode optical fiber with the three-cavity systems' emission and detect the signal using a femtowatt photoreceiver (New Focus 2153) connected to a 12 bits oscilloscope (Tektronix MSO64).

During a single realization of the experiment, the injection beam is first centered onto the considered nanocavity array and subsequently swept over either 20 or 40 nm with different starting wavelengths [as presented in Fig. 2(d) of the main text], depending on the barrier parameter.

APPENDIX E: CHIRAL AND NON-HERMITIAN PARTICLE-HOLE SYMMETRY IN A THREE-CAVITY ARRAY

Chiral symmetry in the context of our disucssion applies to a system consisting of two sublattices A and B, where couplings only take place between two cavities belonging to different sublattices. As long as all the cavities have the same frequency $\tilde{\omega}_0$, the Hamiltonian can be brought to the following form:

$$\tilde{H} = \begin{pmatrix} 0 & T \\ T^\dagger & 0 \end{pmatrix} + \tilde{\omega}_0 \mathbf{1}, \tag{E1}$$

where T is the coupling matrix, † denotes the Hermitian conjugate as usual, and $\mathbf{1}$ is the identity matrix. T can be complex in general, and it is $K \times L$ in size, where K, L are the sizes of the two sublattices. Note that $\tilde{\omega}_0$ does not need to be real, and it is not real in general, due to the cavity decay and material absorption. Nevertheless, by choosing this complex $\tilde{\omega}_0 = \omega_0 - i/\tau$ as the reference frequency or origin of the complex plane, the effective Hamiltonian of the system takes the form

$$\tilde{H} = \begin{pmatrix} 0 & T \\ T^\dagger & 0 \end{pmatrix}, \tag{E2}$$

which is effectively Hermitian. It is straightforward to verify that $\tilde{H}$ given by Eq. (E2) anti-commutes with a diagonal matrix $\mathcal{C}$ consisting of K ones followed by L minus ones, which is often referred as the chiral operator, and therefore the Hamiltonian in Eq. (E2) has chiral symmetry, implying that $\varepsilon_k = -\varepsilon_j$. Let us point out that chiral symmetry can also hold when $\tilde{H}$ is NH, i.e., replacing T by T_1 and $T^\dagger$ by T_2 in Eq. (E2), with $T_2 \neq T_1^\dagger$ [8].

In Fig. 1 of the main text, H is written by arranging the three cavities sequentially. If one wishes to put it in the form of Eq. (E1) in the absence of a pump, one just needs to perform a basis transformation, i.e., exchanging the positions of the second and third cavities:

$$H = \begin{pmatrix} \tilde{\omega}_0 & g & 0 \\ g & \tilde{\omega}_0 & g \\ 0 & g & \tilde{\omega}_0 \end{pmatrix} \to UHU^{-1} = \begin{pmatrix} 0 & 0 & g \\ 0 & 0 & g \\ g & g & 0 \end{pmatrix} + \tilde{\omega}_0 \mathbf{1},$$

$$U = \begin{pmatrix} 1 & 0 & 0 \\ 0 & 0 & 1 \\ 0 & 1 & 0 \end{pmatrix}, \quad T = \begin{pmatrix} g \\ g \end{pmatrix} \in \mathbb{R}.$$

We also note that uniform pumping across the three cavities only changes the value of $\tilde{\omega}_0$ from $\omega_0 - i/\tau$ to $\omega_0 - i(1/\tau - \gamma)$, and hence the system remains effectively Hermitian. Now, if the cavities are pumped non-uniformly, as it is for the case for a (localized) single pump spot, γ will no longer be equal for all of the cavities. As a result, the otherwise chiral symmetry of Eq. (E2) is no longer warranted; NHPH symmetry will hold instead. In such a case, the Hamiltonian anti-commutes with the operator $\mathcal{CT}$, $\mathcal{T}$ being the time-reversal operator. In this case, the eigenvalue spectrum of the Hamiltonian is symmetric about the imaginary axis $\varepsilon_k = -\varepsilon_j^*$.

As mentioned in the main text, both chiral and NHPH symmetries warrant zero modes (when $k = j$), and therefore they constitute sufficient conditions for their existence. However, they are not necessary conditions. Indeed, a zero mode can also exist in the absence of such symmetries. For example, if only cavity 2 in Fig. 1 of the main text is detuned, the Hamiltonian of the system can be written as

$$\tilde{H} = \begin{pmatrix} 0 & 0 & g \\ 0 & 0 & g \\ g & g & \Delta \end{pmatrix}. \tag{E3}$$

This Hamiltonian has neither chiral nor NHPH symmetry as reflected by its eigenvalues,

$$\varepsilon_1 = 0, \quad \varepsilon_{2,3} = \frac{\Delta \pm \sqrt{\Delta^2 + 8g^2}}{2},$$

which are no longer symmetric about the origin or the imaginary axis of the complex plane, independent of whether Δ is real or complex. The zero mode still exists due to "geometric frustration," where the couplings from cavities 1 and 3 are canceled in cavity 2, giving rise to a dark mode. This is particularly the case in our Hermitian resonant scattering experiments (Section 2), where $\Delta = \Delta_0$ above is real. The zero mode then survives. In the NH gain/loss experiments of Sections 3 and 4, we also fulfill this condition when pumping on cavity 2, which changes Δ_0 to $\Delta_0 + i\gamma$. However, the pump has no spatial overlap with the zero mode in this case, and hence the latter cannot be excited or observed. Therefore, strictly speaking, the NH zero mode cannot be linearly excited for nonzero sublattice detuning ($\Delta_0 \neq 0$) under a single pump spot.

An alternative configuration to excite the NH zero mode with nonzero sublattice detuning Δ_0 is to pump cavities 1 and 3 equally, i.e., under a two pump spots configuration, with which Eq. (E3) becomes

$$\tilde{H} = \begin{pmatrix} i\gamma & 0 & g \\ 0 & i\gamma & g \\ g & g & \Delta_0 \end{pmatrix} = \begin{pmatrix} 0 & 0 & g \\ 0 & 0 & g \\ g & g & \Delta_0 - i\gamma \end{pmatrix} + i\gamma \mathbf{1}.$$

Because the term with the identity matrix simply causes a shift of the reference frequency and does not affect the eigenstates of the Hamiltonian, the zero mode survives with Δ now equal to $\Delta_0 - i\gamma$. In this configuration, the pump overlaps perfectly with the zero mode in space, and hence the latter could be excited and observed, even for a large real detuning Δ_0. Importantly, such a two pump spots configuration could lead to zero lasing mode in the three coupled PhC cavities system.

APPENDIX F: ZERO-MODE COALESCENCE AND PHASE TRANSITIONS

In this appendix, we present the full experimental and numerical results as the barrier parameter h is decreased from $h = 0\%$ to $h = -25\%$, i.e., as the intercavity coupling $|g|$ goes from above to below the sublattice detuning $|\Delta\omega|$. Indeed, the NH zero mode is only observed in the $|\Delta\omega| \lesssim |g|$ regime (Fig. 4), while it is missing in the $|\Delta\omega| > |g|$ regime (Fig. 3). First of all, let us recall that, in the large sublattice detuning regime, NHPH symmetry no longer warrants zero modes for single cavity pumping. But, even if M2 loses its symmetry protection, the question arises whether M2 still exists but remains undetectable, or it coalesces through a phase transition. Let us also recall that, in the Hermitian limit, the zero mode is observable for large sublattice detuning [Fig. 2(d), $h = -30\%$, and $h = -35\%$].

The full picture of the different NH phases as a function of the barrier parameter is represented in Fig. 7; this completes the experimental PL maps for various h parameters [Figs. 7(a)–7(e)] and depicts carrier-dependent [Figs. 7(f)–7(j)] as well as linear [Figs. 7(k)–7(o)] CMT calculations. The experimental cases already analyzed in the main text are reproduced in Fig. 7(b) ($h = -20\%$) and in Fig. 7(e) ($h = 0\%$). We identify two phases, corresponding to effective coupling/decoupling of the central cavity with respect to the two extreme ones: the sublattice delocalized phase corresponds to $|\Delta\omega| \lesssim |g|$ ($-5\% \lesssim h \leq 0\%$), in which M2 is observable and becomes the zero mode because of NHPH symmetry; conversely, the sublattice localized phase corresponds to $|\Delta\omega| > |g|$ ($h \leq -10\%$), in which M2 is no longer observable. Interestingly, within this sublattice localized phase, there is a sub-region corresponding to the crossover of g, from positive to negative, vanishing at $h \approx -15\%$. At such a crossover, M1 and M3 exchange symmetries, in the sense that M1 goes from a quasi-symmetric mode with zero phase jumps between the cavities for $g > 0$ to a quasi-symmetric mode with π phase flips between the cavities for $g < 0$. Importantly, within the localized phase, we identify a PT symmetry breaking phase for small $|g|$ [Figs. 7(l) and 7(m)]. CMT calculations show that M2 and M3 merge together at EPs for $-18\% \leq h \leq -11\%$. Such a broken PT-symmetry phase is observable as long as $|g|$ is smaller than $\sim 0.1\Delta\omega$. Let us also point out that, within this very small $|g|$ region, a CMT model with only first neighbor coupling might break down, and second neighbor coupling might be necessary to be taken into account.

We note that in a large array (with more than three cavities), it is possible to induce multiple NH zero modes. The mechanism at work here is the following: the first pair of modes that coalesce at an EP on the imaginary axis and subsequently

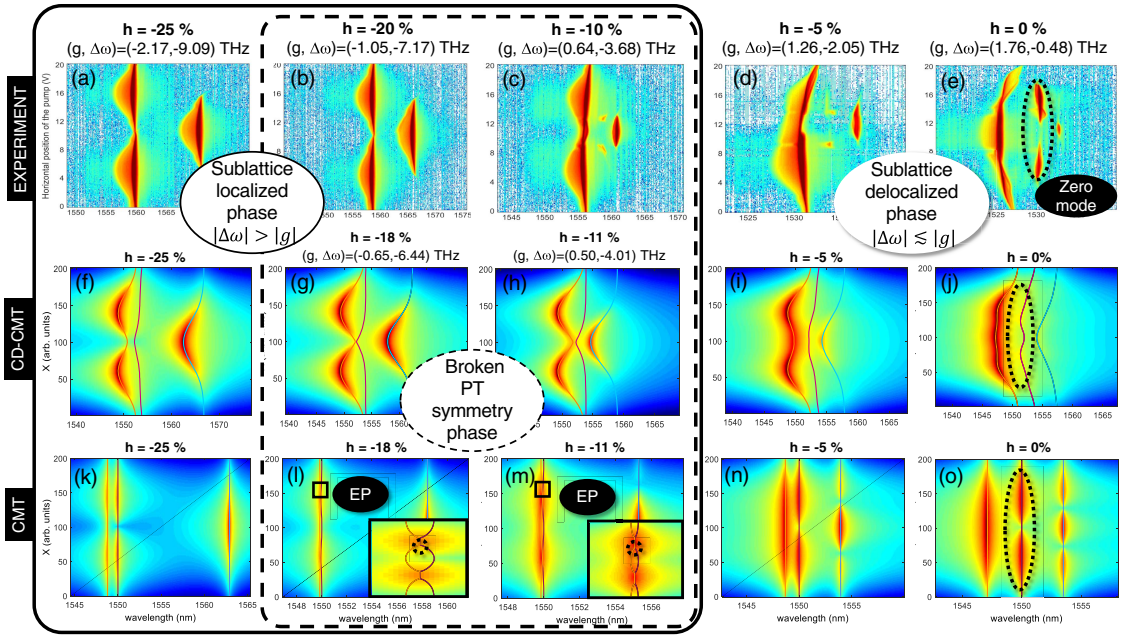

Fig. 7. Phase diagram underlying the transition from sublattice delocalization and zero modes to sublattice localization and mode coalescence. (a)–(e) Experimental PL intensity maps under pump spot position scanning across the coupled cavity system. (a)–(c) $a = 416$ nm, $P_{\text{pump}} = 0.8$ μW; (d), (e) $a = 408$ nm, $P_{\text{pump}} = 1.1$ μW. (f)–(j) CD-CMT and (k)–(o) linear CMT calculations with parameters $\alpha_H = 3$, $\sigma = 40$. (f)–(h) $N = 0.23$, (i) $N = 0.24$, and (j) $N = 0.27$; (k)–(m) $\gamma = 1$, (n) $\gamma = 1.1$, and (o) $\gamma = 1.3$.

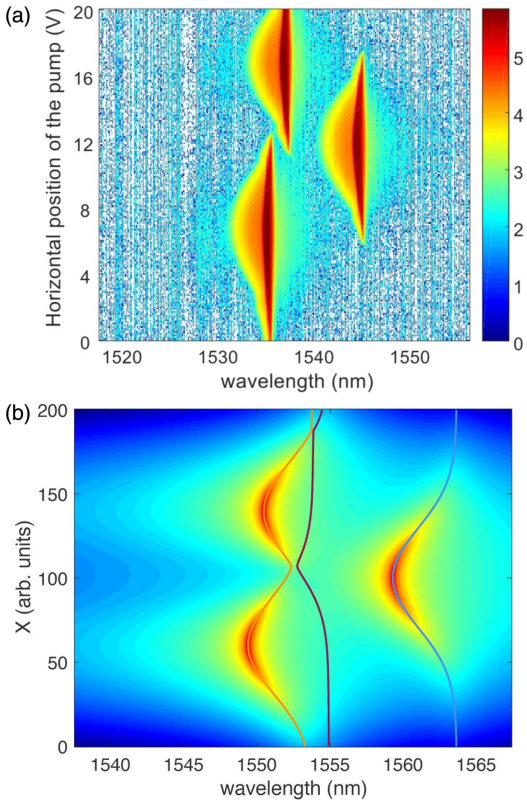

Fig. 8. Zero-mode extinction due to full decoupling. (a) Experimental result on a sample with $h = -20\%$ featuring fabrication imperfections. A detuning of about 1 nm is observed between the extreme cavities. Notice that although three modes are observed around a pump position of 12 V, the three modes are localized into each cavity featuring different frequencies. The middle cavity is decoupled from the extreme one because of large negative h (localized phase). (b) CD-CMT simulations with $h = -20\%$, $N = 0.225$, $\alpha_H = 3$, $\sigma = 40$, and the cavity centered at $x = 140$ is red-detuned by $-6\tau^{-1}$, equivalent to $\Delta\lambda \sim 1.08$ nm.

evolve into two zero modes depends on the spatial profile of the gain, including both its central position and spatial extension. Therefore, by tailing the spatial profile of the gain (or, more practically, the pump), we can coerce different pairs of modes to emerge as NH zero modes on the imaginary axis, with distinct spatial profiles that are correlated with that of the gain.

Finally, notice that the "middle eigenmode" in a linear coupled cavity array is not necessarily a zero mode, for instance, in the case of arbitrarily detuned cavities. The middle eigenmode energy will be mostly localized in a single cavity, whereas the zero mode is delocalized in a sublattice—in the three-cavity example, given by the two extreme cavities. We have observed this situation in many samples, especially for large sublattice detuning, where the two extreme cavities become essentially decoupled from the middle one; furthermore, additional disorder-induced detuning of the two extreme cavities leads to the results depicted in Fig. 8. Here, the barrier parameter is $h = -20\%$, ensuring large sublattice detuning ($\Delta\omega = -7$ THz), and an additional detuning of about 1 nm is observed between the two leftmost intensity maxima in Fig. 8(a), most likely corresponding to a fabrication-induced perturbation. In the model CD-CMT calculations of Fig. 8, this corresponds to a detuning of $\Delta\omega_{13} = 6\tau^{-1}$ between the two extreme cavities; as a result, the three cavities become essentially decoupled. Although at around a pump spot position of 12 V in Fig. 8(a), three modes can be observed in the spectrum, and the middle one is not a zero mode. Note that the model predicts (real part of) eigenvalue crossing because of the carrier-induced blue shift in Fig. 8(b); therefore, the modes behave as if they are not seeing each other.

Funding. National Science Foundation (PHY-1847240); European Commission (MSCA-841351); Agence Nationale de la Recherche (ANR UNIQ DS078, ANR-10-LABX-0035).

Acknowledgment. B. G. and A. M. Y. acknowledge the financial support from the European Union in the form of Marie Skłodowska-Curie Action. L.G. acknowledges support by NSF. This work has also received funding from the European Research Council (ERC) under the Horizon 2020 research and innovation programme (HYPNOTIC PROJECT Grant Agreement No. 726420).

Disclosures. The authors declare no conflicts of interest.

Data Availability. Data underlying the results presented in this paper are not publicly available at this time but may be obtained from the authors upon reasonable request.

REFERENCES

1. M. Z. Hasan and C. L. Kane, "Colloquium: topological insulators," Rev. Mod. Phys. **82**, 3045–3067 (2010).
2. X.-L. Qi and S.-C. Zhang, "Topological insulators and superconductors," Rev. Mod. Phys. **83**, 1057–1110 (2011).
3. J. Alicea, "New directions in the pursuit of Majorana fermions in solid state systems," Rep. Prog. Phys. **75**, 076501 (2012).
4. C. Beenakker, "Random-matrix theory of Majorana fermions and topological superconductors," Rev. Mod. Phys. **87**, 1037–1066 (2015).
5. C. Nayak, S. H. Simon, A. Stern, M. Freedman, and S. Das Sarma, "Non-Abelian anyons and topological quantum computation," Rev. Mod. Phys. **80**, 1083–1159 (2008).
6. J. D. H. Rivero and L. Ge, "Chiral symmetry in non-Hermitian systems: product rule and Clifford algebra," Phys. Rev. B **103**, 014111 (2021).
7. L. Feng, R. El-Ganainy, and L. Ge, "Non-Hermitian photonics based on parity–time symmetry," Nat. Photonics **11**, 752–762 (2017).
8. L. Ge, "Symmetry-protected zero-mode laser with a tunable spatial profile," Phys. Rev. A **95**, 023812 (2017).
9. S. Malzard, C. Poli, and H. Schomerus, "Topologically protected defect states in open photonic systems with non-Hermitian charge-conjugation and parity-time symmetry," Phys. Rev. Lett. **115**, 200402 (2015).
10. J. D. Rivero and L. Ge, "Pseudochirality: a manifestation of Noether's theorem in non-Hermitian systems," Phys. Rev. Lett. **125**, 083902 (2020).
11. M. A. Bandres, S. Wittek, G. Harari, M. Parto, J. Ren, M. Segev, D. N. Christodoulides, and M. Khajavikhan, "Topological insulator laser: experiments," Science **359**, eaar4005 (2018).
12. H. Zhao, X. Qiao, T. Wu, B. Midya, S. Longhi, and L. Feng, "Non-Hermitian topological light steering," Science **365**, 1163–1166 (2019).
13. C. Poli, M. Bellec, U. Kuhl, F. Mortessagne, and H. Schomerus, "Selective enhancement of topologically induced interface states in a dielectric resonator chain," Nat. Commun. **6**, 7710 (2015).
14. H. Zhao, P. Miao, M. H. Teimourpour, S. Malzard, R. El-Ganainy, H. Schomerus, and L. Feng, "Topological hybrid silicon microlasers," Nat. Commun. **9**, 981 (2018).

15. W. Song, W. Sun, C. Chen, Q. Song, S. Xiao, S. Zhu, and T. Li, "Breakup and recovery of topological zero modes in finite non-Hermitian optical lattices," Phys. Rev. Lett. **123**, 165701 (2019).
16. M. Pan, H. Zhao, P. Miao, S. Longhi, and L. Feng, "Photonic zero mode in a non-Hermitian photonic lattice," Nat. Commun. **9**, 1308 (2018).
17. P. Hamel, S. Haddadi, F. Raineri, P. Monnier, G. Beaudoin, I. Sagnes, A. Levenson, and A. M. Yacomotti, "Spontaneous mirror-symmetry breaking in coupled photonic-crystal nanolasers," Nat. Photonics **9**, 311–315 (2015).
18. S. Haddadi, P. Hamel, G. Beaudoin, I. Sagnes, C. Sauvan, P. Lalanne, J. A. Levenson, and A. M. Yacomotti, "Photonic molecules: tailoring the coupling strength and sign," Opt. Express **22**, 12359–12368 (2014).
19. D. Pellegrino, P. Busi, F. Pagliano, B. Romeira, F. W. van Otten, A. Y. Silov, and A. Fiore, "Mode-field switching of nanolasers," APL Photon. **5**, 066109 (2020).
20. K.-H. Kim, M.-S. Hwang, H.-R. Kim, J.-H. Choi, Y.-S. No, and H.-G. Park, "Direct observation of exceptional points in coupled photonic-crystal lasers with asymmetric optical gains," Nat. Commun. **7**, 13893 (2016).
21. K. Takata, K. Nozaki, E. Kuramochi, S. Matsuo, K. Takeda, T. Fujii, S. Kita, A. Shinya, and M. Notomi, "Observing exceptional point degeneracy of radiation with electrically pumped photonic crystal coupled-nanocavity lasers," Optica **8**, 184–192 (2021).
22. B. Qi, L. Zhang, and L. Ge, "Defect states emerging from a non-Hermitian flatband of photonic zero modes," Phys. Rev. Lett. **120**, 093901 (2018).
23. P. Lalanne, W. Yan, K. Vynck, C. Sauvan, and J.-P. Hugonin, "Light interaction with photonic and plasmonic resonances," Laser Photon. Rev. **12**, 1700113 (2018).
24. K. A. Atlasov, K. F. Karlsson, A. Rudra, B. Dwir, and E. Kapon, "Wavelength and loss splitting in directly coupled photonic-crystal defect microcavities," Opt. Express **16**, 16255–16264 (2008).
25. Y. Akahane, T. Asano, B.-S. Song, and S. Noda, "High-*Q* photonic nanocavity in a two-dimensional photonic crystal," Nature **425**, 944–947 (2003).
26. N.-V.-Q. Tran, S. Combrié, and A. De Rossi, "Directive emission from high-*Q* photonic crystal cavities through band folding," Phys. Rev. B **79**, 041101 (2009).
27. S. Haddadi, A. M. Yacomotti, I. Sagnes, F. Raineri, G. Beaudoin, L. Le Gratiet, and J. A. Levenson, "Photonic crystal coupled cavities with increased beaming and free space coupling efficiency," Appl. Phys. Lett. **102**, 011107 (2013).
28. B. Garbin, J. Fatome, G.-L. Oppo, M. Erkintalo, S. G. Murdoch, and S. Coen, "Asymmetric balance in symmetry breaking," Phys. Rev. Res. **2**, 023244 (2020).
29. L. Ge, "Parity-time symmetry in a flat-band system," Phys. Rev. A **92**, 052103 (2015).
30. C. Tradonsky, I. Gershenzon, V. Pal, R. Chriki, A. A. Friesem, O. Raz, and N. Davidson, "Rapid laser solver for the phase retrieval problem," Sci. Adv. **5**, eaax4530 (2019).
31. Z. Zhang, X. Qiao, B. Midya, K. Liu, J. Sun, T. Wu, W. Liu, R. Agarwal, J. M. Jornet, S. Longhi, N. M. Litchinitser, and L. Feng, "Tunable topological charge vortex microlaser," Science **368**, 760–763 (2020).